Journal of Materials Chemistry B

PAPER

Cite this: J. Mater. Chem. B, 2015, 3, 5341

Hetero-nanocomposites of magnetic and antifungal nanoparticles as a platform for magnetomechanical stress induction in *Saccharomyces cerevisiae*†

K. Giannousi,[a] M. Menelaou,[a] J. Arvanitidis,[b] M. Angelakeris,[b] A. Pantazaki[c] and C. Dendrinou-Samara*[a]

Received 20th April 2015,
Accepted 26th May 2015

DOI: 10.1039/c5tb00734h

www.rsc.org/MaterialsB

Copper(I) oxide (Cu_2O) nanoparticles (NPs) of 30 nm with antifungal properties have been functionalized with 9 nm nickel ferrite ($NiFe_2O_4$) magnetic nanoparticles (MNPs) to construct hetero-nanocomposites (NCs) of a submicron hydrodynamic size for magnetomechanical stress induction in the yeast, *Saccharomyces cerevisiae*. A post-synthetic approach involving the assembly through hydrophobic interactions of the preformed NPs of non-uniform sizes, albeit coated with the same surfactant (oleylamine), is reported. Solvents of different polarity were implemented during the synthetic procedure resulting in NCs of similar composition consisting mainly of MNPs randomly decorated onto the bigger Cu_2O NPs. The antifungal properties of the building NPs and the NCs were studied in terms of fungistatic and fungicidal activity, whereas the ionic leaching was found to be negligible, highlighting the nanosize effect. Although *S. cerevisiae* cells were found to be resistant to individual $NiFe_2O_4$ MNPs because of their small size, their sensitivity to NCs significantly increased upon short-time exposure to a rotating low-frequency magnetic field (10 min, 30 Hz, 35 G) and this arises from the collective properties. The magnetomechanical cell stress induction was accompanied by alteration of cellular membrane integrity and programmed cell death signaling.

Introduction

The vast development of single nanoparticles (NPs) in the past decade enabled us to create the second generation of nanoscale materials, namely nanocomposites (NCs) that refers to the assemblies of hetero- or homo-nanoparticles structures with variable properties. The interest in these materials derives from the collective properties resulting from the adequate designation of the primary units as well as from the unique characteristics of the heterostructure itself that allows their application in fields such as catalysis,[1] optoelectronic applications,[2] biological detection,[3] theranostics[4] and solar energy conversion.[5] For example, by combining inorganic NPs with magnetic and plasmonic features into one hetero-nanostructure, distinct effects can be achieved simultaneously, while cooperatively enhanced performances, based upon tuning the exchange interaction at a magnetically hard–soft interface, may also be accomplished if the necessary ingredients are incorporated.

In general the preparation of multicomponent nanostructures can be achieved by using one-pot synthesis and/or by post-synthetic methods while the borderline between them is not always clear. In both ways, control over the particle size distribution and homogeneity still remains challenging.[6] The main idea in one-pot synthesis comes from the typical procedure for isolating, bimetallic NPs, namely the seed mediated approach. This procedure is quite popular for a number of heterostructures while it has been well established for the synthesis of semiconductor quantum dots (QDs) with epitaxial shells.[7] Gold-iron(II,III) oxide (Au–Fe_3O_4) heterostructured NPs are among the most studied bi-functional materials that have been synthesized *in situ* for several purposes, for example, to act as computed tomography and magnetic resonance imaging enhancing contrast agents;[4] to study their plasmonic properties,[8] to selectively induce apoptosis in cancer cells and to be used in real-time imaging.[9] Furthermore, Nikolic *et al.* reported the synthesis of bi-magnetic composites Fe_3O_4-manganese ferrite ($MnFe_2O_4$) with improved magnetic properties.[10] NCs incorporating copper(I) oxide (Cu_2O) NPs, with and without magnetic constituents have also been studied for various technological and medical applications.[11]

[a] Laboratory of Inorganic Chemistry, Department of Chemistry, Aristotle University of Thessaloniki, 54124 Thessaloniki, Greece. E-mail: samkat@chem.auth.gr
[b] Department of Physics, Aristotle University of Thessaloniki, Thessaloniki, Greece
[c] Laboratory of Biochemistry, Department of Chemistry, Aristotle University of Thessaloniki, Thessaloniki, Greece

† Electronic supplementary information (ESI) available. See DOI: 10.1039/c5tb00734h

Fe_3O_4–Cu_2O NCs were prepared using one-step *in situ* polymerization for use as an absorbent in water treatment,[12] whereas M–Cu_2O (where M = silver, Au) revealed enhanced photocatalytic activity.[13] Additionally, core–shell systems such as Cu_2O–copper(II) oxide (CuO) NCs that were isolated using the thermal reduction of the CuO,[14] and NCs of Cu_2O–Cu with a flower-like architecture have been prepared using a template free solvent-thermal route,[15] and showed improved photocatalytic activity.

Concerning post-synthetic methods, the separate preparation of single units was superseded by organization of homo/hetero NPs introduced either from interparticle interactions resulting in assemblies[16] or through polymer encapsulation leading to colloidal superparticles (SPs).[17] The organization of NPs in SPs demonstrated by Menelaou *et al.*[18] gave rise to size- and shape-controlled assemblies with promising biomedical applications. Also, less developed approaches have been reported, for example, Bao *et al.* isolated Au–Fe_3O_4 NCs using chemical bond linkage to study their efficiency in protein separation,[19] whereas Choi *et al.*, in an attempt to combine QDs and magnetic NPs, used the hydrophobic interaction between Fe_3O_4–ZnS/silver–indium–sulfide with oleylamine (OAm).[20]

This study was motivated by the emerging concept of hetero-nanocomposites *via* a post-synthetic approach of functionalizing non-magnetic NPs with magnetic NPs through hydrophobic interactions. A simple synthetic route is reported in which the magnetic features of $NiFe_2O_4$ NPs are combined with the antifungal properties of Cu_2O NPs and to the best of our knowledge it is the first time that such an NCs system, namely, $NiFe_2O_4$–Cu_2O, as a two-fold platform with dual action involving magneto-mechanical cell stress therapy and antifungal activity has been reported. Cu-based NPs have been explored previously as antimicrobial agents by Giannousi *et al.*[21] and others,[22] and have been proven to exhibit enhanced biological activity, therefore offering new possibilities for biomedical research. Previously, it was found that 30 nm Cu_2O NPs possessed enhanced antifungal and antibacterial activity and specificity against Gram-positive strains of these organisms, whereas their activity is exerted *via* the production of reactive oxygen species and the nanosized composition effect is predominant.[21] As far as the magnetic component is concerned, magnetic microdiscs[23] and colloidal SPs from nanocubes in the submicron region[24] have been explored for use in nanobiomagnetic applications, including magnetomechanical treatment. Most experimental work up to now has used superparamagnetic particles with typically small values of the magnetization of saturation, resulting in the requirement of high magnetic fields in order to manipulate them. $NiFe_2O_4$ NPs can act as agents to induce a magnetomotive force in the presence of a low frequency magnetic field, because they possess size-dependent soft magnetic features, mild high frequency degradation and enhanced performance in hyperthermia therapy.[25] In connection with their cytotoxic effects, the size of the NPs is presented as the crucial factor affecting the cell proliferation, with the larger NPs showing a higher cytotoxicity. $NiFe_2O_4$ NPs of 20–30 nm decreased HeLa (human cervical adenocarcinoma) cell viability at concentration as high as 100 μg mL^{-1},[26] whereas Neuro-2A (mouse neuroblast) cell viability was not significantly affected by 100 μg mL^{-1} of 10 nm $NiFe_2O_4$ NPs.[27]

In this research, NC synthesis was designed on the basis of a driven assembly by using non-uniform size building units of 9 nm $NiFe_2O_4$ and 30 nm Cu_2O good-shaped NPs with the same coating and with improved magnetic and antifungal properties, respectively. The collective properties in terms of magnetization and antifungal activity were also exploited. The detailed characterization of the NCs was implemented using a series of complementary experimental techniques [X-ray powder diffraction (XRD), transmission electron microscopy (TEM), scanning electron microscopy (SEM), elemental mapping, dynamic light scattering (DLS), Fourier-transform infrared (FT-IR) and Raman spectroscopy, thermogravimetric analysis (TGA), and vibrating sample magnetometry (VSM)]. Eventually, the magnetomechanical effect of NCs on the yeast, *Saccharomyces cerevisiae*, a unicellular eukaryotic model microorganism used in molecular and cell biology,[28] was examined. The fungistatic and fungicidal activity of the NCs was investigated initially in the absence of a magnetic field and afterwards with short-time exposure to a rotating low frequency magnetic field (10 min, 30 Hz, 35 G), while the cell morphology and membrane integrity were evaluated by optical fluorescence microscopy.

Experimental

Materials

Copper(II) nitrate trihydrate (Merck, ≥99.5%, M = 241.60 g mol^{-1}, >$Cu(NO_3)_2{\cdot}3H_2O$), hydrazine hydrate (Merck, ~100%, M = 50.06 g mol^{-1}, $N_2H_4{\cdot}H_2O$), oleylamine (Sigma-Aldrich, 70%, M = 267.49 g mol^{-1}, OAm), diphenyl ether (Sigma-Aldrich, ≥99%) and nickel(II) acetylacetonate (Riedel-de Haën, ≥99.9%, M = 256.91 g mol^{-1}, $Ni(acac)_2$) were of analytical grade and were used without any further purification. Agarose (BRL), tryptone, yeast extract (Oxoid, Hampshire, UK), fluorescein diacetate (FDA, 3,6-diacetoxyfluoran) (Sigma). Solvents were used without any further purification and were purchased from Sigma-Aldrich.

Synthesis of NCs

The synthetic procedure of $NiFe_2O_4$@Cu_2O NCs consists of three separate stages:

Stage 1: solvothermal synthesis of $NiFe_2O_4$@OAm single nanoparticles. $NiFe_2O_4$@OAm NPs were solvothermally prepared according to a previous report by Menelaou *et al.*[29] Briefly, 1.8 mmol of iron(III) acetylacetonate ($Fe(acac)_3$) and 0.9 mmol of $Ni(acac)_2$ were dissolved in OAm. The resulting solution was transferred into a 23 mL Teflon-lined stainless steel autoclave which was placed in an oven and the temperature was increased up to 200 °C for 24 h. The resulting product was washed with ethanol and $NiFe_2O_4$@OAm NPs were obtained.

Stage 2: solvothermal synthesis of Cu_2O@OAm single nanoparticles. Cu_2O@OAm NPs were obtained using a previous method of Giannousi *et al.*,[30] where 4.1 mmol of $Cu(NO_3)_2{\cdot}3H_2O$ was dissolved in 4 mL of deionized water, 4.1 mmol of $N_2H_4{\cdot}H_2O$ (0.2 g) and 6 mL of OAm were all added to the

mixture which was then placed into a Teflon-lined stainless steel autoclave. Crystallization was carried out under autogenous pressure at 200 °C for 24 h and then the NPs were isolated after centrifugation.

Stage 3: general synthesis of $NiFe_2O_4$@Cu_2O NCs. The as-prepared $NiFe_2O_4$@OAm (20 mg) NPs were dissolved in 5 mL of toluene and a solution of Cu_2O@OAm (20 mg) NPs in 1 mL dimethyl sulfoxide (DMSO) was added. The resulting mixture was heated at 50 °C for 24 h with vigorous stirring. After that slow evaporation of toluene followed and ethanol was added to the reduced solution. The mixture was centrifuged at 1000 rpm where the supernatant liquid was discarded and a brown precipitate was obtained (sample NC-1). Sample NC-2 was prepared using the same procedure but the $NiFe_2O_4$@OAm NPs were dissolved in chloroform ($CHCl_3$) and 5 mL of OAm was added to the starting mixture. Sample NC-3 was prepared using the same procedure as sample NC-1 but acetonitrile (CH_3CN) was used to dissolve the $NiFe_2O_4$@OAm NPs. In all cases the precipitants (NC-1, NC-2, NC-3) were washed thoroughly with toluene or $CHCl_3$ or CH_3CN, respectively, and ethanol at least three times to remove the monomers.

Characterization techniques

XRD measurements were performed using a two-cycle Rigaku Ultima + diffractometer (40 kV, 30 mA, Cu-Kα radiation) with Bragg–Brentano geometry (detection limit approximately 2%). Conventional TEM images were obtained using a JEOL 100CX microscope, operating at an acceleration voltage of 100 kV. For TEM observations suspensions of the NCs deposited onto carbon-coated copper TEM grids were used. FT-IR spectroscopy analysis results were recorded using a Nicolet FT-IR 6700 spectrometer with KBr pellets in the range of 350–4000 cm^{-1}. TGA was performed using a SETARAM SETSYS-1200 and carried out in the temperature range from room temperature to 850 °C at a heating rate of 10 °C min^{-1} under a nitrogen (N_2) atmosphere. Magnetic measurements were performed at 300 K in a Oxford Instruments 1.2H/CF/HT VSM as function of the applied field (up to 1 T). The elemental composition of the samples was determined using SEM with a Jeol 840A microscope. Raman spectra were recorded in the backscattering geometry using an HORIBA LabRAM ARAMIS spectrometer equipped with a Peltier cooled charge-coupled detector. For the excitation, the 532 nm line of a diode laser was focused on the samples using a 100× objective at a power lower than 0.1 mW, to avoid any laser heating induced effects. Graphite furnace atomic absorption spectrometry (GFAAS) was performed using a PerkinElmer HGA 900 graphite furnace to measure the ionic release. The dynamic light scattering (DLS) measurements were performed using a Malvern Instruments Zetasizer analyzer.

Ninhydrin colorimetric assay. The presence of free amine groups on the surface of the single components and the NCs was detected using a ninhydrin colorimetric assay. Aliquots of OAm (0.1–0.6 mL; 0.25 mg mL^{-1}) in *N*,*N*-dimethylformamide (DMF) were pipetted into a series of tubes.[31] To each tube, ninhydrin solution in methanol (0.06 mL, 0.7 mL, 10.7 mg mL^{-1}) was added, and the mixture was mixed well and heated in a water bath at 100 °C for 5 min. After heating, the tubes were left to cool, and then the contents were transferred to a 5 mL volumetric flask, and the volume was adjusted with DMF, and the ultraviolet/visible (UV/Vis) absorbance at 450–900 nm was measured. A series of the NPs/NCs in DMF (0.25 mg mL^{-1}) was prepared accordingly, and each sample of stock solution (0.4 mL) was pipetted into boiling tubes with ninhydrin solution (0.7 mL) following the same procedure described for OAm and subsequently UV/Vis measurements of the complex formed were performed.

Biological studies

Antifungal activity studies. The yeast, *S. cerevisiae* was used as a model organism to screen the antifungal properties of the newly prepared NPs/NCs. The cultivation medium used for antifungal activity test was the minimal medium salts broth (MMS). It contained 1.5% (w/v) glucose, 0.5% (w/v) ammonium chloride, 0.5% (w/v) dipotassium phosphate, 0.1% (w/v) sodium chloride, 0.01% (w/v) magnesium sulfate heptahydrate, and 0.1% (w/v) yeast extract. The pH of the medium was adjusted to 7.0. A series of different pre-cultures were prepared, where each of them consisted of 20 mL of MMS inoculated with 3 mg of the yeast, *S. cerevisiae*. Subsequently, the pre-cultures grown at the optimal growth temperature (30 °C) until the middle of exponential phase were separated in to 2 mL aliquots. To the first group of aliquots, various concentrations of NPs/NCs were added to reach final concentrations of 2.5, 5, 10, 25, 50, and 100 μg mL^{-1} in NPs/NCs. The stock solutions of the NPs/NCs (2.5 mg mL^{-1}) were prepared by dissolving them in distilled water. A second group of the same cultures, supplemented with suitable concentrations of the NPs/NCs but devoid of inoculums, was tested as well. These cultures were prepared to monitor any possible presence of fungus or microorganisms able to grow in this medium. A third group of cultures, supplemented with inoculum but devoid of NPs/NCs, was also used, which indicated the fungal growth profile in the absence of NPs/NCs (reference cultures). All the cultures were incubated at 30 °C for 22 h. Fungal growth was measured as the increase in absorbance at 600 nm and determined using a Thermo Electron Corporation Helios γ spectrophotometer (USA). In the percentage calculation of growth inhibition of the yeast, *S. cerevisiae* resulting from the presence of NPs/NCs, the absorbance values for the reference cultures were considered as 100% growth. The minimum inhibitory concentration (MIC) in μg mL^{-1}, defined as the lowest concentration of a compound or material that inhibits 50% of the growth (IC_{50} value) of an organism,[32] was determined based on the inhibition growth of the batch cultures, containing varying concentrations of the NPs/NCs in suspension.[33,34]

Fungus viability. The fungus viability in the absence and the presence of various concentrations of NPs/NCs was also estimated by determining the degree of enzymatic hydrolysis of FDA by *S. cerevisiae* cultures. In detail, FDA is cleaved to fluorescein and acetic acid by different enzymes, such as proteases, lipases, and esterases. These enzymes are constituents of the primary metabolism of fungi and microorganisms.[35] The released fluorescein was measured using a fluorescence spectrophotometer.

A stock solution of fluorescein diacetate in acetone (2 mg mL^{-1}) to reach a final FDA concentration of 10 μg mL^{-1} was added in two series of *S. cerevisiae* cultures already grown to the middle of the exponential phase, in the absence and presence of various concentrations of NPs/NCs. These cultures were incubated at 30 °C on a rotary shaker (120 rpm) for 1 h in total. After intervals of 15 min, 1 mL aliquots were taken from the cultures and placed in Eppendorf tubes. The hydrolysis of FDA was terminated by addition of acetone to reach a final acetone concentration of 50% v/v.[35] The mixture was centrifuged for 5 min in a LaboGene ScanSpeed 1236MG multipurpose centrifuge, at 10 000 rpm to remove suspended particles, and finally the fluorescence was measured.

Based on the above screening of the antifungal activity of the samples, it was decided to expose to the rotating low frequency magnetic field (30 Hz, 35 G) those cells that were treated overnight for 22 h with either $NiFe_2O_4$ NPs or with NCs of 100 μg mL^{-1}. Yeast cells devoid of NPs/NCs were also exposed to the magnetic field whereas isolated Cu_2O NPs were excluded from this study, because they do not possess net magnetization. After 10 min of exposure to the magnetic field, the cells were allowed to recover for 2 h under standard conditions. The growth inhibition and fungal viability were estimated by the two methods described previously.

***S. cerevisiae* genomic DNA isolation and fungal DNA fragmentation in agarose gel electrophoresis.** Details of the analytical procedure used are given elsewhere.[30] The *S. cerevisiae* genomic DNA isolation supervened the exposure of the cells with NPs/NCs to the magnetic field.

Imaging of nanoparticles and cells. Optical fluorescence microscopy images were obtained using an Optika B-500 TiFL with an HBO illumination system, trioncular epi-fluorescence microscope equipped with a digital camera set (DIGI, 8 megapixels) with an optical adapter and measuring software. The fluorescence was measured at λ_{ex} = 475 nm and λ_{em} = 535 nm.

Results and discussion

Single $NiFe_2O_4$ magnetic nanoparticles (MNPs) were functionalized onto Cu_2O NPs using hydrophobic interactions resulting in the formation of heterogeneous NCs namely NC-1, NC-2 and NC-3. The former hydrophobic building NPs, $NiFe_2O_4$@OAm and Cu_2O@OAm were of much different sizes, 9 nm and 30 nm respectively, whereas they were coated with the same surfactant. The assembly process took place by attractive Van der Waals forces and/or hydrogen bonding through evaporation and when the reduction of the available volume occurred. The order in the NCs was determined by the polarity of the solvents whereas the concentration of the NPs remained constant. Thus, three solvents of different polarity and dielectric constant were implemented for the solubilization of the MNPs and Cu_2O@OAm was dissolved, in all cases, in the same solvent, DMSO. Extra OAm was used with NC-2 to explore if its presence during synthesis could further stabilize the NCs.

In the XRD patterns (Fig. 1) of the synthesized NCs (NC-1, NC-2, NC-3), diffraction peaks with the presence of both $NiFe_2O_4$ and Cu_2O, having different relative intensities, are presented. XRD patterns of building the NPs with crystallographic details are given in the ESI,† Fig. S1. In order to extract the composition of each sample, as well as the corresponding values of the lattice parameters, the diffractograms were fitted using the Le Bail analysis[36] using the FullProf program[37] (Fig. 1) and are summarized in Table 1. The lattice parameters are similar when compared to those of single $NiFe_2O_4$ NPs (a = 8.339 Å)[29] and Cu_2O NPs (a = 4.28 Å)[30] as opposed to binary superlattices, where the values of lattice parameters are increased significantly.[38]

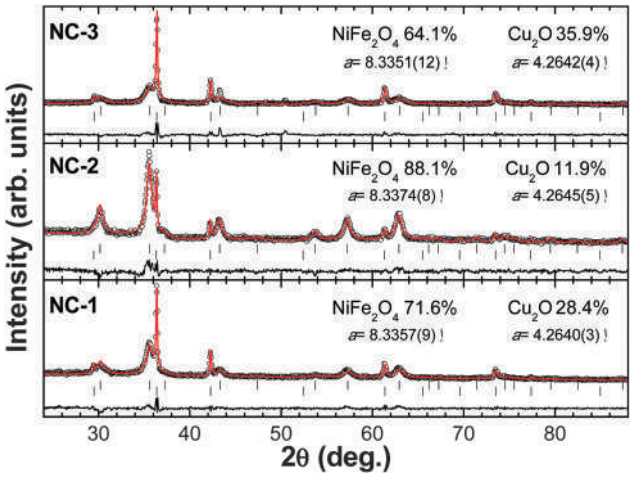

Fig. 1 Le Bail fits (red lines) of the NC-1, NC-2 and NC-3 samples. The composition of each sample and the lattice parameters are also included in the figure.

Table 1 Overview of the magneto-structural features of NC-1, NC-2 and NC-3

	NC-1	NC-2	NC-3
Composition by Le Bail analysis (%$NiFe_2O_4$/%Cu_2O)	71.6/28.4	88.1/11.9	64.1/35.9
$a_{NiFe_2O_4}$ (Å)	8.3357(9)	8.3374(9)	8.3351(12)
$\%R_{wp}$	4.09	4.09	4.69
$\%R_{exp}$	2.44	2.19	2.81
a_{Cu_2O} (Å)	4.2640(3)	4.2645(5)	4.2642(4)
$\%R_{wp}$	4.88	4.98	4.51
$\%R_{exp}$	2.40	2.26	2.10
M_s (emu g^{-1})	26	35	25
H_c (Oe)	180	150	164

Representative images of NC-1 (Fig. 2a) and NC-2 (Fig. 2b) obtained using SEM are presented in Fig. 2(I), whereas the results of the energy-dispersive X-ray spectroscopy (EDS) analysis illustrating the peaks of Cu, Fe and Ni elements, are shown in Fig. 2(II). Further, elemental mapping using the SEM-EDS technique was also performed. The elemental mapping corresponding to the areas illustrated in Fig. 2(III) is depicted in different colors for Cu (red), Fe (blue) and Ni (yellow), and revealed the spatial uniformity of the element distribution in both NCs.

The morphology of the preformed NPs and the NCs was studied using TEM. The shape of both $NiFe_2O_4$ (Fig. 3(a)) and

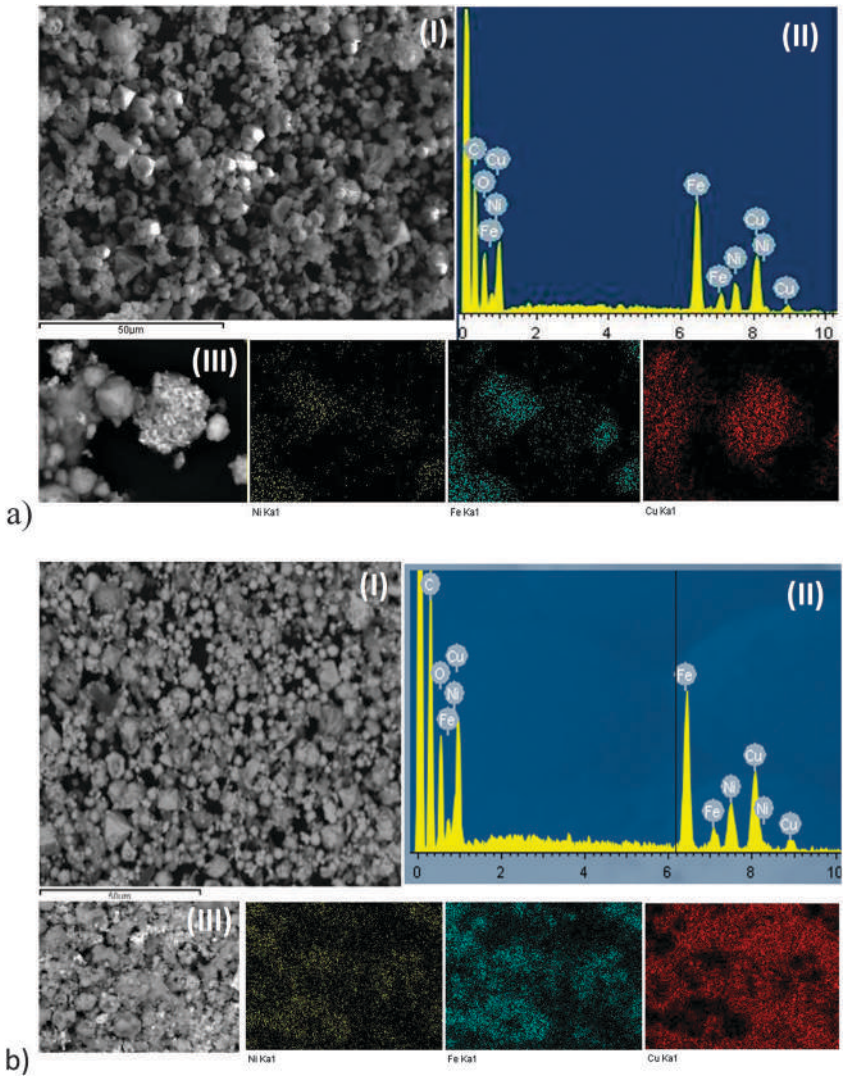

Fig. 2 (I) SEM images of (a) the as prepared NC-1, and (b) NC-2. (II) EDS spectra of (a) NC-1, (b) NC-2. (III) SEM elemental mapping of Cu, Fe and Ni in (a) NC-1 and (b) NC-2.

Cu_2O NPs (Fig. 3(b)) is nearly spherical, and a big difference in their size is recorded with the former NPs being 9 nm and the latter 30 nm. The NCs consist mainly of larger Cu_2O NPs surrounded by smaller spherical $NiFe_2O_4$ NPs as shown in Fig. 3(c)–(e). It is evident that their morphology is highly dependent on the shape of the building NPs with no significant changes attributed to the synthetic approach used. The uneven decoration of larger Cu_2O NPs with the smaller MNPs is observed and no regular assembly or epitaxial structure can be seen.

Based on the structural characterization, NCs of different composition were isolated. The phase ratio of the MNPs is higher in all cases than the Cu_2O NPs, which is attributed to the spontaneous self-assembly (Gibbs free energy (ΔG) < 0) driven by the significant size difference between the MNPs and Cu_2O NPs. As the system tries to minimize its free energy thermodynamically, direct interparticle interactions unfold that originate from Van der Waals forces, hydrogen bonding and/or entropic effects.[39] Meanwhile, the diffusion coefficient is lower for the smaller particles resulting in the bigger particles being surrounded by many smaller ones. No significant difference in composition was found when the aprotic solvent, toluene, was used (NC-1) instead of the polar solvent CH_3CN (NC-3) indicating that the assemblies are mainly influenced by the different sizes of NPs contrary to the generation of superlattices where the polarity of the solvents led to a different order.[16] However, the addition of extra OAm was favorable towards $NiFe_2O_4$ NPs because these are present in a much higher percentage compared to the Cu_2O phase in sample NC-2.

Raman spectra in the frequency region of 250–750 cm^{-1} were acquired to further verify the microstructure of the NC-1 and NC-2 samples (spectra 3 and 5 in Fig. 4), and the spectra of the individual components of $NiFe_2O_4$ NPs and Cu_2O NPs were also recorded for the estimation of the composition of the NCs (spectra 1 and 2 in Fig. 4). More specifically, because $NiFe_2O_4$ crystallizes in the spinel structure of space group $Fd\bar{3}m$, the group theoretical calculations predict five Raman active bands,

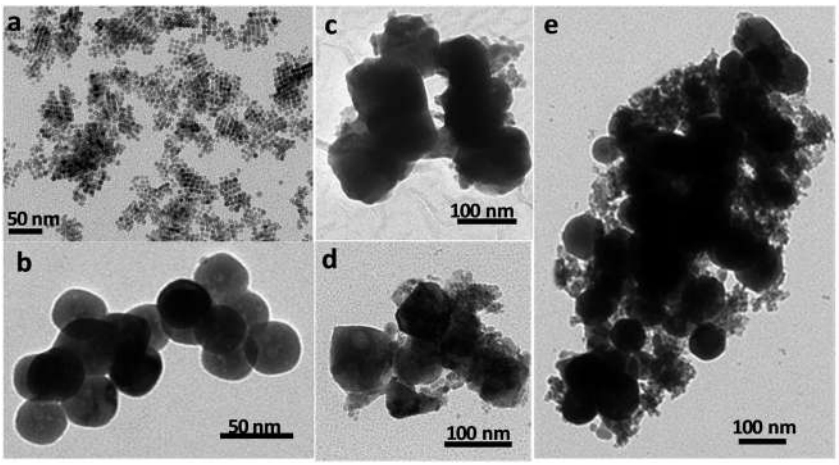

Fig. 3 TEM images of (a) $NiFe_2O_4$ NPs, (b) Cu_2O NPs, (c) the as prepared NC-1, (d) NC-3 and (e) NC-2.

which belong to the irreducible representations: $\Gamma = A_{1g} + E_g + 3T_{2g}$.[40] In the Raman spectrum included in the lower panel of Fig. 4, the bands appearing at ~335, 487, 580 and ~703 cm^{-1} are attributed to the E_g, T_{2g}, T_{2g} and A_{1g} modes, respectively. Contrary to the archetypal Fe_3O_4 spinel system, the coexistence of Fe and Ni in the octahedral sites of $NiFe_2O_4$ and the concomitant bond length distribution causes the shoulder-like features at the lower frequency side of the Raman active bands.[41,42] On the other hand, Cu_2O crystallizes in the cuprite structure (space group: $Pn\bar{3}m$), having only one Raman active mode at ~520 cm^{-1} of the T_{2g} symmetry.[43] The other Raman bands appearing in spectrum 2 of Fig. 4 originate from infrared active or silent modes. This breakdown of the selection rules in Cu_2O is ascribed to defects, non-stoichiometry, and to the resonant excitation.[44]

In order to estimate the composition of the NC-1 and NC-2 from the Raman data, an attempt was made to reproduce their spectra (spectra 3 and 5) assuming appropriate contributions from those of the individual components (spectra 1 and 2). The calculated spectra are also included in Fig. 4 (spectra 4 and 6). The similarity between spectrum 4 and 6 with spectrum 3 and 5, respectively, is apparent, suggesting a composition of 64% $NiFe_2O_4$ – 36% Cu_2O for NC-1 and 70% $NiFe_2O_4$ – 30% Cu_2O for NC-2, which is in fair agreement with the results of the XRD analysis.

The total amount of weight loss was determined using TGA by measuring the mass reduction in the range of 100–850 °C and is equal to 27.4 wt% and 26.7 wt% for the single particles of $NiFe_2O_4$@OAm and Cu_2O@OAm, respectively, and 28.0 wt% and 29.5 wt% for NC-1 and NC-2, respectively (Fig. 5). The decomposition of $NiFe_2O_4$@OAm sample occurs up to a temperature of approximately 600 °C, which strongly supports the suggestion that a double layer of OAm molecules is formed during the synthetic procedure, surrounding the $NiFe_2O_4$ NPs. As illustrated in Fig. 5, the decomposition of the organic coating occurs in a similar way for NC-1 and NC-2 and this is comparable with previously reported OAm-capped MNPs.[45]

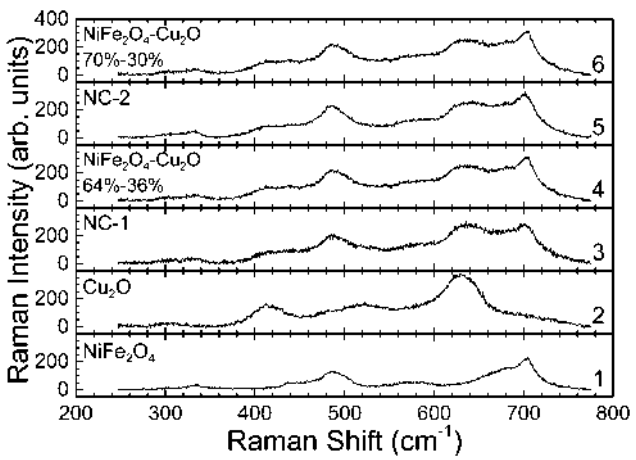

Fig. 4 Raman spectra of the individual components $NiFe_2O_4$ and Cu_2O (spectra 1 and 2) and the NC-1 and NC-2 (spectra 3 and 5). Spectra 4 and 6 are calculated from spectra 1 and 2, assuming contributions of 64–36% and 70–30%, respectively.

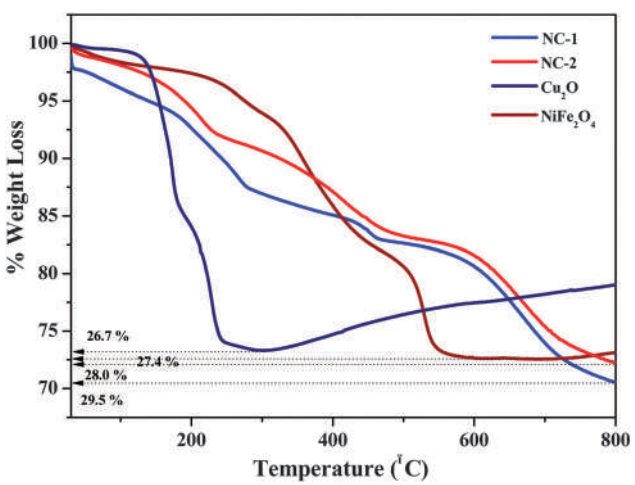

Fig. 5 TGA curves of the OAm-capped $NiFe_2O_4$ and Cu_2O NPs and the nanocomposites (NC-1 and NC-2) under a N_2 flow.

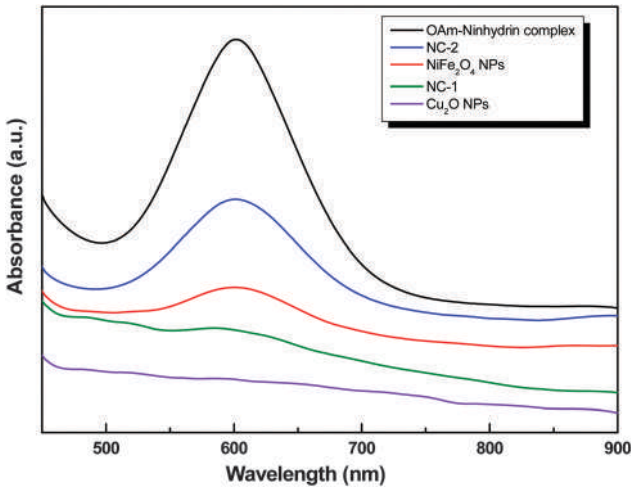

Fig. 6 UV/Vis absorbance spectra of $NiFe_2O_4$ NPs, Cu_2O NPs, NC-1, NC-2 and pure OAm after reaction with ninhydrin.

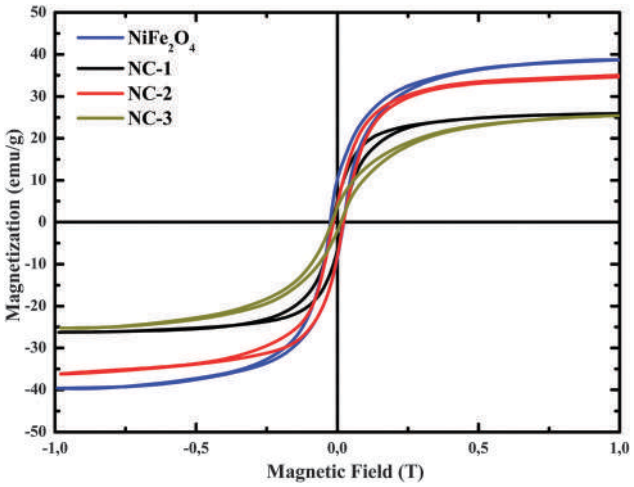

Fig. 7 VSM measurements of $NiFe_2O_4$ NPs, NC-1, NC-2 and NC-3 at 300 K.

In particular, two main regions of mass reduction were observed: one at 100–235 °C (NC-1) or 100–280 °C (NC-2), where the hydrocarbon chains are removed, and a second step lasting up to ~500 °C, which is associated with the burn off of the amine head groups.

The presence of OAm was certified using FT-IR spectroscopy (ESI,† Fig. S2), whereas the free amine groups of OAm were detected using a ninhydrin colorimetric assay. The measurements were performed in DMF solutions, in which the NPs/NCs showed a good colloidal dispersion. Ninhydrin reacted with the immobilized amine groups of OAm and generated a soluble Ruhemann's purple chromophore, which remained in the supernatant liquid. The absorbance of the Ruhemann's complex with OAm was found at 601 nm, which is fairly consistent with the λ_{max} of the complex in DMF. The results presented in Fig. 6 verify the presence of free amines in the case of the primary $NiFe_2O_4$ NPs, NC-2 and NC-1, whereas based on the calibration curve prepared for OAm (ESI,† Fig. S3), the respective values for the NH_2 groups were calculated as 4.82 μg mL^{-1}, 9.23 μg mL^{-1} and 0.8 μg mL^{-1}, respectively. In the case of Cu_2O NPs free amine groups (NH_2) were negligible, indicating bonding with the metal core. Taking into account that the initial MNPs were covered by double layer of OAm molecules, the stabilization of NCs was derived by hydrophobic interactions of the hydrocarbon chains of Cu_2O@OAm NPs when compared to those of the $NiFe_2O_4$@OAm NPs, whereas the presence of free amines (NC-1) is coming from MNPs and for NC-2 is higher because of the extra OAm that has been used for the preparation. The system can be considered to be similar to the well-known functionalization of organic coating onto hydrophobic NPs.

The magnetic properties of the single particles of MNPs as well as of the NC-1, NC-2 and NC-3 were carried out at room temperature using a VSM with an applied field of 10 kOe. The room temperature hysteresis loops (Fig. 7) for all the samples revealed the characteristic behavior of soft magnetic materials, which is in accordance with the presence of $NiFe_2O_4$ NPs in all the samples. The saturation magnetization (M_s) value of the $NiFe_2O_4$ NPs is 39.0 emu g^{-1}, while the M_s of the NC-1, NC-2 and NC-3 decrease to ~26.0 emu g^{-1}, 35.0 emu g^{-1} and 25.0 emu g^{-1}, respectively. In addition, the coercivity field is 235 Oe for $NiFe_2O_4$ NPs whereas it is 180 Oe, ~150 Oe and 164 Oe for NC-1, NC-2 and NC-3, respectively (Table 1). The magnetization and the coercivity field reduction from the single particles of $NiFe_2O_4$ to the NCs can be attributed to the presence of the Cu_2O NPs in the latter. Furthermore, the difference in the magnetization and coercivity field among the NCs can be attributed to two synergistic factors: (a) the different ratio between $NiFe_2O_4$ and Cu_2O in the composites (as calculated using the Le Bail method) and (b) the variations in the synthetic route used for the isolation of the samples and in particular the addition of extra OAm during the synthesis of NC-2 which was found to be crucial since it has been reported that amine ligands which act as σ-donors, such as OAm, can increase the spin–orbit coupling because of a decrease of the crystal field splitting which favors the uplift of the magnetocrystalline anisotropy of the surface layer.[46] Therefore, the higher magnetic component present in sample NC-2 results in more pronounced collective magnetic features than for the other two NCs when compared to $NiFe_2O_4$ NPs.

Antifungal activity of NPs

The synthesized NCs were examined for their use as mechanical stress mediators. *S. cerevisiae* cells were used as a unicellular eukaryotic model system to evaluate the efficacy of the nanostructure-based magnetomechanical stress therapy. In this treatment, NCs were initially injected into cells and after 22 h of incubation, these samples were subjected to an external rotating magnetic field (10 min, 30 Hz, 35 G) forcing the NCs to follow the field rotation, and thus generate mechanical forces on the targeted cells, activating specific cell responses and potentially leading to cell destruction and death. Initially, the antifungal activity of each component and the NCs (average of three measurements) were studied in a concentration- and time-dependent manner (ESI,† Fig. S4). Following 22 h of incubation

Table 2 Antifungal activity of the NPs and the NCs, evaluated using the half-minimal inhibitory concentration (IC_{50} in μg mL^{-1})

Samples	IC_{50} growth (μg mL^{-1}) (optical density A_{600nm})
Cu_2O NPs	34.75 ± 1.42
$NiFe_2O_4$ NPs	>100
NC-1	76.67 ± 2.04
NC-2	97.56 ± 2.58

with the NPs, the MIC values (IC_{50}), which refer to the fungal growth (optical density) were calculated and are summarized in Table 2. Two controls were also included in the procedure: fungal cells without NPs and fungal cells with the respective organic coating of the NPs. The low IC_{50} value recorded for Cu_2O NPs (34.75 μg mL^{-1}) confirmed the significant fungal growth inhibition, and this result was in accordance with results from a previous study.[30] However, the *S. cerevisiae* cells were found to be resistant to the $NiFe_2O_4$ NPs even after 22 h of incubation (IC_{50} = >100 μg mL^{-1}) and this result was in agreement with results from cytotoxicity studies using 10 nm $NiFe_2O_4$ NPs in a Neuro-2A cell line.[27] The IC_{50} values recorded for the $NiFe_2O_4$@Cu_2O nanostructures (NC-1: 76.67 μg mL^{-1}, NC-2: 97.56 μg mL^{-1}) indicated an intermediate effect on the yeast growth. Leaching tests were performed using GFAAS for the highest concentration of NPs/NCs (100 μg mL^{-1}) both in H_2O and the culture medium after 22 h of incubation and the ionic release was found to be beyond the resolution limit of the device (<0.5 μg L^{-1}). Consequently, the antifungal activity of $NiFe_2O_4$@Cu_2O heterostructures is attributed not only to the presence of Cu_2O NPs but also to their nanosize and shape.

The antifungal activity (average of three measurements) of the single $NiFe_2O_4$ and Cu_2O NPs, as well as the NCs towards *S. cerevisiae* was also estimated in terms of viability using the fluorescence method, which could better distinguish between viable and lysed cells. In detail, the fungal viability was estimated by determining the degree of esterase activity of *S. cerevisiae* cells. FDA was used as a substrate because it is enzymatically cleaved into fluorescein and acetic acid when the fungus is metabolically active. The fluorescein released was measured using fluorescence spectrometry and the results are shown in Fig. 8. The highest release was demonstrated in the controls. After adding 100 μg mL^{-1} of the primary NPs and/or NCs to the cultures and incubating for 22 h, the total esterase activity was affected, indicating that the viability of the fungi was decreased. More specifically, the resistance of *S. cerevisiae* cells to the $NiFe_2O_4$ NPs and their sensitivity to the Cu_2O NPs were further confirmed because the fungal viability was found to be 81% and 14% compared to control, respectively. In the presence of the NCs, cell death was also recorded with the viability rates being 33% and 47% for NC-1 and NC-2, respectively.

Based on the previous screening of the antifungal activity of the samples, it was decided to expose those cells that were treated overnight (22 h) either with MNPs or with NCs of 100 μg mL^{-1}, to the magnetic field. Isolated Cu_2O NPs were excluded from this study, because they do not possess net magnetization. After 10 min of exposure to the 30 Hz magnetic field, the cells were allowed to recover for 2 h under standard conditions. The growth inhibition and the fungal viability were determined using optical density and fluorescence measurements, respectively, and these showed that the magnetic field did not cause measurable growth inhibition/death of the cells without the NPs or the NCs (Fig. 9 and 10) but induced considerable growth inhibition/death of the cells containing either MNPs or NCs. Meanwhile, the temperature of the samples remotely monitored by a thermal camera always remained below ~22 °C during these experiments and varied no more than a few degrees during magnetic field exposure, and in this way hyperthermia was excluded as a possible mechanism of cell destruction. Meanwhile, DLS measurements in phosphate buffered saline were carried out that showed the monodispersity of NCs, whereas the mean hydrodynamic size values were 923.6 nm and 842.3 nm for NC-1 and NC-2, respectively (ESI,† Fig. S5). Looking at these results and taking into account the cells that were

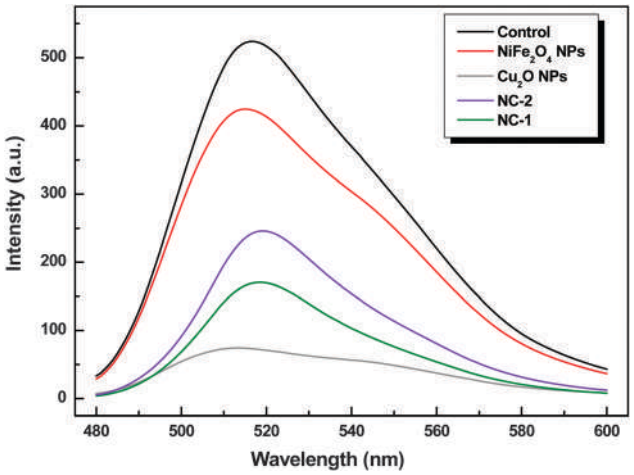

Fig. 8 Viability of *S. cerevisiae* cells in the presence of $NiFe_2O_4$ NPs (red line), Cu_2O NPs (gray line), NC-1 (olive line) and NC-2 (magenta line). The black line is the control. The concentration of the NPs/NCs added at the logarithmic growth phase was 100 μg mL^{-1}. Fluorescence was measured at λ_{ex} = 455 nm and $\lambda_{em\ max}$ = 515 nm.

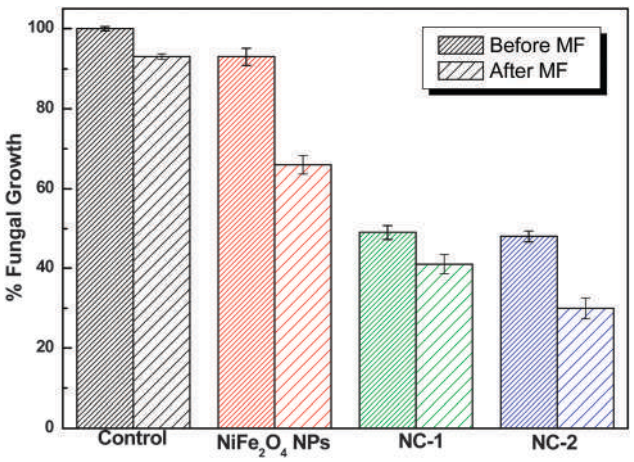

Fig. 9 Comparative percentage fungal growth before and after the exposure of *S. cerevisiae* cells without NPs/NCs (black), with $NiFe_2O_4$ NPs (red), NC-1 (green) and NC-2 (blue) to the 30 Hz magnetic field (MF).

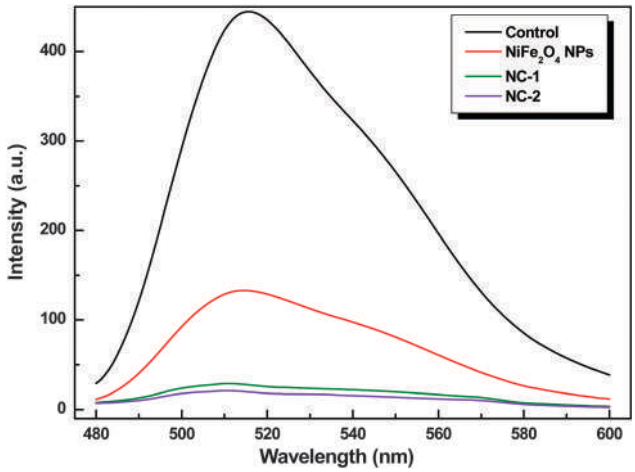

Fig. 10 Viability of *S. cerevisiae* cells in the presence of $NiFe_2O_4$ NPs (red line), NC-1 (olive line) and NC-2 (magenta line) after exposure to the 30 Hz MF. The black line is the control. The concentration of the NPs/NCs added at the logarithmic growth phase was 100 μg mL^{-1}. Fluorescence was measured at λ_{ex} = 455 nm and $\lambda_{em\ max}$ = 515 nm.

not exposed to the magnetic field, it can be concluded that their submicron size in addition to the magnetic field exposure was essential for NP/NC-induced cell destruction.

As depicted in Fig. 9, the efficacy of the NPs/NCs towards the fungus was affected by the magnetic field with respect to their M_s values. Magnetomechanical treatment with $NiFe_2O_4$ NPs, which displayed the higher M_s value, resulted in 35% growth inhibition and 70% cell death, whereas without exposure to the magnetic field the rates were 7% and 19% for NPs and NCs, respectively. The M_s value of NC-2 was higher than that for NC-1 and therefore the inhibition rate was more prominent in the former case (70%) than in the latter case (59%). In the absence of the magnetic field the fungal growth was inhibited up to 52% in both cases. The fluorescence measurements (Fig. 10) proved that magnetomechanical treatment with NC-1 and NC-2 was effective and caused 93.7% and 95.5% cell death, respectively.

Cell morphology changes after magnetic field application were observed using a fluorescence microcopy, because the metabolically active fungal cells would enzymically convert the non-fluorescent FDA into the green fluorescent fluorescein compound. Fig. 11 compares the representative images of the control cells with cells after 30 Hz magnetic field exposure following 22 h of culture under standard conditions. For the untreated cells the round shape of the cells and the cell wall/membrane integrity are observed. Furthermore, the fluorescence is located exclusively in the cell contour, attributed possibly to the FDA hydrolysis by activity of the periplasmic esterases.[47] Contrary to this, the treated cells present irregular shapes, with loss of membrane integrity, indicating that the magnetomechanical effects can be attributed partly to the perturbations of the cellular membrane integrity. The internalization of NPs into the fungus cells as dark clusters concomitant with an abundant cytoplasmic vacuolization is obvious.

The size- and shape-dependent antimicrobial activity and membrane damage of the NPs has been extensively reported and it is well-established that particles of small hydrodynamic size with uneven surfaces and edges are biologically more reactive.[48] The submicron size and the irregular shape with edges of the NCs (indicated by TEM images) do not allow their internalization through simple diffusion, ion channels or *via* endocytosis, suggesting that the most possible mechanism is the direct physical interaction.[49] The magnetic forces drive the NCs to the *S. cerevisiae* cell membranes and in that way they become damaged, as indicated by the deep holes observed in Fig. 11, and the NCs act in a similar way as the previously reported ferromagnetic microdisks[23] and chitosan functionalized submicron disks towards cancer cells.[50] However, the force produced by slowly oscillating NCs on the cell surface could not alone cause such profound effects. Disruption of plasma membrane integrity is characteristic of oncotic cells but

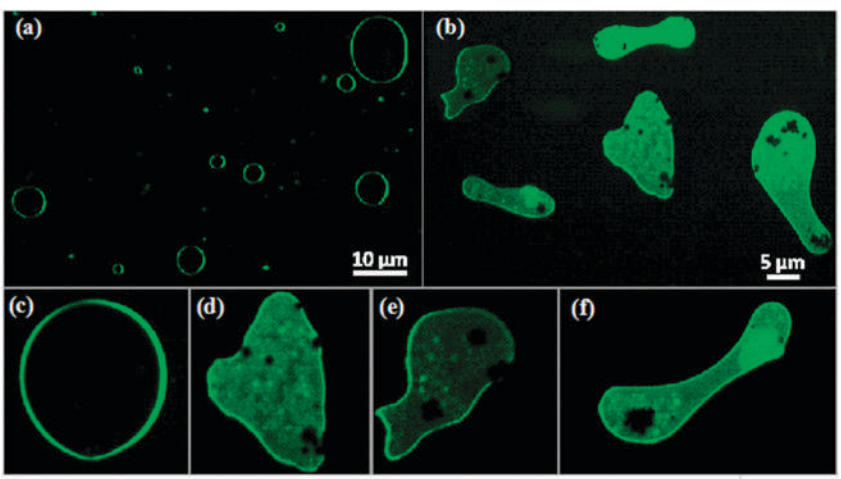

Fig. 11 Optical fluorescence microscopy images of *S. cerevisiae* cells (a) in the absence of NPs/NCs (control) or (b) in the presence of NC-2 (b) and higher magnification (40×) images of (c) control cells and (d–f) cells treated with NC-2 after their exposure to the 30 Hz magnetic field. Fluorescence was measured at λ_{ex} = 475 nm and λ_{em} = 535 nm.

also of late apoptotic cells.[51] The proposed term ''oncosis'' used in cell death is accompanied by cellular and organelle swelling, cytoplasmic vacuolization, blebbing and disintegration of the cell membranes. Therefore, it is feasible that the observed effects have not resulted from membrane rupture alone, but instead are because of the triggering of intracellular pathways activating programmed cell death through application of the magnetic field in combination with the antifungal activity of Cu_2O NPs. Additional evidence for the induction of programmed cell death is derived from the DNA fragmentation observed using electrophoresis of genomic DNA (ESI,† Fig. S6).[52] DNA was isolated from the fungal cells treated with NC-1, NC-2 and MNPs after their exposure to the magnetic field, whereas the effect of Cu_2O NPs on the DNA was also included. DNA fragmentation is reflected in all cases in the long smearing effect of the DNA tail which is because of the DNA degradation products separated all along the gel. The near disappearance of the band of NC-2 (lane 5), which corresponds to almost complete DNA degradation, is in fair agreement with the enhanced antifungal activity recorded after the exposure of the cells to the magnetic field. However, further investigation is needed to elucidate the mechanism of action at the molecular level.

Conclusions

A post-synthetic approach is presented for the functionalization of single, relatively large, Cu_2O particles (30 nm) with small $NiFe_2O_4$ NPs (9 nm). The assembly can be considered as an expansion of the already known functionalization of NPs with an additional organic coating from the hydrophobic interactions. Indeed, in the present study an additional inorganic carrier was added and hetero-NCs resulted. Despite the drawback of the uneven decoration of the NCs, effective assemblies were still formed. However, further investigation is needed concerning the different concentrations and/or morphology of the starting building NPs that may result in a more precisely controlled assembly. The antifungal activity of Cu_2O NPs was significantly improved by their decoration with MNPs upon exposure to a low frequency magnetic field, because magneto-mechanical cell stress induction was achieved. The underlying mechanism of action was proved to involve perturbations of the cellular membrane integrity and triggering of programmed cell death. Apart from these encouraging results opening up new opportunities for tracking the mechanotransduction signaling, both at the subcellular and molecular level, the measurement of magnetomechanical properties is still challenging, because it restricts both the design of new products and the performance of smart devices.

Acknowledgements

This research was co-financed by the European Union (European Social Fund – ESF) and Greek national funds through the Operational Program ''Education and Lifelong Learning'' of the National Strategic Reference Framework (NSRF) – Research Funding Program: THALES – Investing in Knowledge Society through the European Social Fund.

References

1 T. Yu, J. Zeng, B. Lim and Y. N. Xia, *Adv. Mater.*, 2010, **22**, 5188–5192.
2 J. T. Zhang, Y. Tang, K. Lee and M. Ouyang, *Nature*, 2010, **466**, 91–95.
3 S. H. Choi, H. B. Na, Y. I. Park, K. An, S. G. Kwon, Y. Jang, M. Park, J. Moon, J. S. Son, I. C. Song, W. K. Moon and T. Hyeon, *J. Am. Chem. Soc.*, 2008, **130**, 15573–15580.
4 J. Zhu, Y. Lu, Y. Li, J. Jiang, L. Cheng, Z. Liu, L. Guo, Y. Pan and H. Gu, *Nanoscale*, 2014, **6**, 199–202.
5 I. Thomann, B. A. Pinaud, Z. Chen, B. M. Clemens, T. F. Jaramillo and M. L. Brongersma, *Nano Lett.*, 2011, **11**, 3440–3446.
6 (*a*) W. Shi, H. Zeng, Y. Sahoo, T. Y. Ohulchansky, Y. Ding, Z. L. Wang, M. Swihart and P. N. Prasad, *Nano Lett.*, 2006, **6**, 875–881; (*b*) J. Xie, F. Zhang, M. Aronova, L. Zhu, X. Lin, Q. Quan, G. Liu, G. Zhang, K.-Y. Choi, K. Kim, X. Sun, S. Lee, S. Sun, R. Leapman and X. Chen, *ACS Nano*, 2011, **5**, 3043–3051.
7 S. Behrens, *Nanoscale*, 2011, **3**, 877–892.
8 A. Mezni, I. Balti, A. Mlayah, N. Jouini and L. S. Smiri, *J. Phys. Chem. C*, 2013, **117**, 16166–16174.
9 W. Gao, L. Ji, L. Li, G. Cui, K. Xu, P. Li and B. Tang, *Biomaterials*, 2012, **33**, 3710–3718.
10 A. S. Nikolic, M. Boskovic, V. Spasojevic, B. Jancar and B. Antic, *Mater. Lett.*, 2014, **120**, 86–89.
11 *Metallic Nanomaterials*, ed. C. S. S. R. Kumar, Wiley-VCH Verlag GmbH & Co. KGaA, Weinheim, Germany, 2009.
12 J. Cao, J. Li, L. Liu, A. Xie, S. Li, L. Qiu, Y. Yuana and Y. Shen, *J. Mater. Chem. A*, 2014, **2**, 7953–7959.
13 Z. Wang, S. Zhao, S. Zhu, Y. Sun and M. Fang, *CrystEngComm*, 2011, **13**, 2262–2267.
14 C. Wang, Y. Wang, X. Liu, F. Diao, L. Yuanc and G. Zhouc, *Phys. Chem. Chem. Phys.*, 2014, **16**, 17487–17492.
15 B. Zhou, H. Wang, Z. Liu, Y. Yang, X. Huang, Z. Lü, Y. Sui and W. Su, *Mater. Chem. Phys.*, 2011, **126**, 847–852.
16 L. Xu, W. Ma, L. Wang, C. Xu, H. Kuang and N. A. Kotov, *Chem. Soc. Rev.*, 2013, **42**, 3114–3126.
17 (*a*) T. Wang, D. LaMontagne, J. Lynch, J. Zhuang and Y. C. Cao, *Chem. Soc. Rev.*, 2013, **42**, 2804–2823; (*b*) Y. Xia, Z. Tang. X. Zhang, J. Han and T. Yao, *Chem. Commun.*, 2012, **48**, 6320–6336; (*c*) J. Wu, H. Zhang, H. Zhang, X. Zhang and B. Yang, *CrystEngComm*, 2011, **13**, 5674.
18 M. Menelaou, Z. Iatridi, I. Tsougos, K. Vasiou, C. Dendrinou-Samara and G. Bokias, *Dalton Trans*, 2015, DOI: 10.1039/C5DT00372E.
19 J. Bao, W. Chen, T. Liu, Y. Zhu, P. Jin, L. Wang, J. Liu, Y. Wei and Y. Li, *ACS Nano*, 2007, **1**, 293–298.
20 K. S. Choi, B. K. Bang, P. K. Bae, Y.-R. C. Kim and H. Kim, *J. Nanosci. Nanotechnol.*, 2013, **13**, 1820–1823.
21 (*a*) K. Giannousi, I. Avramidis and C. Dendrinou-Samara, *RSC Adv.*, 2013, **3**, 21743–21752; (*b*) K. Giannousi, K. Lafazanis,

J. Arvanitidis, A. Pantazaki and C. Dendrinou-Samara, *J. Inorg. Biochem.*, 2014, **133**, 24–32.

22 (*a*) A. K. Chatterjee, R. Chakraborty and T. Basu, *Nanotechnology*, 2014, **25**, 135101; (*b*) V. Vellora, T. Padil and M. Černík, *Int. J. Nanomed.*, 2013, **8**, 889–898; (*c*) H. Pang, F. Gao and Q. Lu, *Chem. Commun.*, 2009, 1076–1078.

23 D.-H. E. Kim, A. Rozhkova, I. V. S. Ulasov, D. Bader, T. Rajh, M. S. Lesniak and V. Novosad, *Nat. Mater.*, 2010, **9**, 165–171.

24 T. Wang, X. Wang, D. LaMontagne, Z. Wang, Z. Wang and Y. C. Cao, *J. Am. Chem. Soc.*, 2012, **134**, 18225–18228.

25 G. Stefanou, D. Sakellari, K. Simeonidis, Th. Kalabaliki, M. Angelakeris, C. Dendrinou-Samara and O. Kalogirou, *IEEE Trans.*, 2014, **50**, 6872577.

26 A. Tomitaka, A. Hirukawa, T. Yamada, S. Morishita and Y. Takemura, *J. Magn. Magn. Mater.*, 2009, **321**, 1482–1484.

27 H. Yin, H. P. Too and G. M. Chow, *Biomaterials*, 2005, **26**, 5818–5826.

28 T. Nomura, J. Miyazaki, A. Miyamoto, Y. Kuriyama, H. Tokumoto and Y. Konishi, *Environ. Sci. Technol.*, 2013, **47**, 3417–3423.

29 M. Menelaou, K. Georgoula, K. Simeonidis and C. Dendrinou-Samara, *Dalton Trans.*, 2014, **43**, 3626–3636.

30 K. Giannousi, G. Sarafidis, S. Mourdikoudis, A. Pantazaki and C. Dendrinou-Samara, *Inorg. Chem.*, 2014, **53**, 9657–9666.

31 V. Georgiadou and C. Dendrinou-Samara, *Eur. J. Inorg. Chem.*, 2014, 3645–3656.

32 A. K. Suresh, D. A. Pelletier and M. J. Doktycz, *Nanoscale*, 2013, **5**, 463–474.

33 M. A. Tsiaggali, E. G. Andreadou, A. G. Hatzidimitriou, A. A. Pantazaki and P. Aslanidis, *J. Inorg. Biochem.*, 2013, **121**, 121–128.

34 D. N. Williams, S. H. Ehrman and T. R. P. Holoman, *J. Nanobiotechnol.*, 2006, **4**, 3.

35 P. Verma, J. Dyckmans, H. Militz and C. Mai, *Appl. Microbiol. Biotechnol.*, 2008, **80**, 125–133.

36 A. Le Bail, H. Duroy and J. L. Fourquet, *Mater. Res. Bull.*, 1998, **23**, 447.

37 J. Rodriquez-Carvajal, *Physica B*, 1993, **192**, 55.

38 (*a*) F. X. Redl, K.-S. Cho, C. B. Murray and S. O'Brien, *Nature*, 2003, **423**, 968–971; (*b*) E. V. Shevchenko, D. V. Talapin, N. A. Kotov, S. O'Brien and C. B. Murray, *Nature*, 2006, **439**, 55–59.

39 M. Grzelczak, J. Vermant, E. M. Furst and L. M. Liz-Marzán, *ACS Nano*, 2010, **4**, 3591–3605.

40 J. Kreisel, G. Lucazeau and H. Vincent, *J. Solid State Chem.*, 1998, **137**, 127.

41 A. Ahlawat and V. G. Sathe, *J. Raman Spectrosc.*, 2011, **42**, 1087–1094.

42 Z. H. Zhou, J. M. Xue and J. Wang, *J. Appl. Phys.*, 2002, **91**, 6015.

43 L. Debbichi, M. C. Marco de Lucas, J. F. Pierson and P. Krüger, *J. Phys. Chem. C*, 2012, **116**, 10232–10237.

44 (*a*) A. Compaan and H. Z. Cummins, *Phys. Rev. B: Condens. Matter Mater. Phys.*, 1972, **6**, 4753–4757; (*b*) K. Reimann and K. Syassen, *Phys. Rev. B: Condens. Matter Mater. Phys.*, 1989, **39**, 11113–11119.

45 M. Menelaou, K. Georgoula, K. Simeonidis and C. Dendrinou-Samara, *Dalton Trans.*, 2014, **43**, 3626–3636.

46 (*a*) N. Cordente, M. Respaud, F. Senocq, M.-J. Casanove, C. Amiens and B. Chaudret, *Nano Lett.*, 2001, **1**, 565–568; (*b*) C. R. Vestal and Z. J. Zhang, *J. Am. Chem. Soc.*, 2003, **125**, 9828–9833; (*c*) J. Mohapatra, A. Mitra, D. Bahadur and M. Aslam, *CrystEngComm*, 2013, **15**, 524–532.

47 G. E. Wheeler and A. H. Rose, *J. Gen. Microbiol.*, 1973, **74**, 189–192.

48 (*a*) A. K. Suresh, D. A. Pelletier and M. J. Doktycz, *Nanoscale*, 2013, **5**, 463–474; (*b*) G. Applerot, J. Lellouche, A. Lipovsky, Y. Nitzan, R. Lubart, A. Gedanken and E. Banin, *Small*, 2012, **8**, 3326–3337; (*c*) J. Agudo-Canalejo and R. Lipowsky, *ACS Nano*, 2015, **9**, 3704–3720.

49 (*a*) A. Elsaesser and C. V. Howard, *Adv. Drug Delivery Rev.*, 2012, **64**, 129–137; (*b*) Y.-N. Chang, M. Zhang, L. Xia, J. Zhang and G. Xing, *Materials*, 2012, **5**, 2850–2871.

50 D.-H. Kim, P. Karavayev, E. A. Rozhkova, J. Pearson, V. Yefremenko, S. D. Bader and V. Novosad, *J. Mater. Chem.*, 2011, **21**, 8422–8426.

51 (*a*) G. Majno and I. Joris, *Am. J. Pathol.*, 1995, **146**, 3–15; (*b*) M. J. Polanco, L. F. Alguacil and C. González-Martín, *J. Appl. Toxicol.*, 2012, **34**, 19–24.

52 (*a*) F. Z. Shahneh, B. Baradaran, J. Majidi and Z. Babaloo, *Biomed. J.*, 2014, **37**, 298–304; (*b*) Y. Yonezawa, H. Yoshida and Y. Mizushina, *Int. J. Mol. Sci.*, 2007, **8**, 1206–1224.